The 2 December 2020 MW 4.6, Kallithea (Viotia), central Greece earthquake: a very shallow damaging rupture detected by InSAR and its role in strain accommodation by neotectonic normal faults

Sotiris Valkaniotis, Vincenzo de Novellis, Athanassios Ganas, Eugenio Sansosti, Vincenzo Convertito, Pierre Briole, Varvara Tsironi, Ilektra Karasante, Ioannis Karamitros

Acta Geophysica
https://doi.org/10.1007/s11600-023-01213-2

RESEARCH ARTICLE - SOLID EARTH SCIENCES

The 2 December 2020 M_W 4.6, Kallithea (Viotia), central Greece earthquake: a very shallow damaging rupture detected by InSAR and its role in strain accommodation by neotectonic normal faults

Sotiris Valkaniotis[1] · Vincenzo De Novellis[2] · Athanassios Ganas[3] · Eugenio Sansosti[2] · Vincenzo Convertito[4] · Pierre Briole[5] · Varvara Tsironi[3,6] · Ilektra Karasante[7] · Ioannis Karamitros[3]

Received: 16 September 2022 / Accepted: 11 October 2023

Abstract
On 2 December 2020 10:54 UTC a shallow earthquake of M_W (NOA) = 4.6 occurred near the village of Kallithea (to the east of Thiva), central Greece, which, despite its modest size, was locally damaging. Using InSAR and GNSS data, we mapped a permanent change on the ground surface, i.e., a subsidence of 7 cm. Our geodetic inversion modelling indicates that the rupture occurred on a WNW–ESE striking, SSW-dipping normal fault, with a dip-angle of ~ 54°. The maximum slip value was 0.35 m, which was reached at a depth of about 1100 m. The analysis of broadband seismological data also provided kinematic source parameters such as moment magnitude $M_W = 4.6$ (± 0.1), rupture area 6.3 km^2 and mean slip 0.16 m, which agree with the values obtained from the geodetic model. The effects of the earthquake were disproportionate to its moderate magnitude, probably due to its unusually shallow depth (slip centroid at 1.1 km) and the high efficiency of the earthquake (radiation efficiency $\eta = 0.62$). The geodetic data inversion also indicates that within the uncertainty limits of the technique, three scenarios are possible (a) the earthquake responsible for the mapped surface deformation may have occurred on a ~ 2-km long, blind normal fault different from the well-known active Kallithea normal fault or (b) could have occurred along a secondary fault that branches off the Kallithea fault or (c) it may have occurred along the Kallithea fault itself, but with its geometrical configuration could not be modelled with available data. We have also concluded that with a high dip-angle Kallithea Fault forward model it is not possible to fit the geodetic data. The rupture initiated at a very shallow depth (1.1 km) and it could not propagate deeper possibly because of a structural barrier down-dip. The 2020 event near Kallithea highlighted the structural complexity in this region of the Asopos Rift valley as the reactivation of the WNW–ESE structures indicates their significant role in strain accommodation and that they still represent a seismic hazard for this region.

Keywords Earthquake · InSAR · Inversion · Radiation efficiency · Viotia · Greece

Introduction

On 2 December 2020 10:54 UTC a shallow earthquake rocked the hilly areas to the east of Thiva (Thebes), central Greece (Fig. 1; Valkaniotis and Ganas 2020; Elias et al. 2021; Kaviris et al. 2022). The epicentre was located 12 km east of Thiva, about 46 km to the NNW of Athens. The earthquake had a magnitude of $M_W = 4.6$ according to the National Observatory of Athens (NOA 2020) and its maximum intensity was IV (ITSAK instrumental intensity map shown in Fig. S1). Using InSAR and GNSS data, both Valkaniotis and Ganas (2020) and Elias et al. (2021) found out that this moderate event caused an impressive permanent change on the ground surface, that is a permanent subsidence of several centimetres in amplitude. The effects (deformation, shaking) of the earthquake were disproportional to its moderate magnitude, likely because of its unusually shallow depth (centroid depth of 1.6 km; NOA 2020). Given the uniqueness of this event, we were motivated to investigate the rupture plane characteristics and the source parameters using high-quality geodetic data (GNSS and InSAR) and broadband seismic waveforms. Compared to the study by Elias et al. (2021), we have included in our processing two more GNSS stations in our processing, namely 014A (a HEPOS station; Gianniou 2010) and KALI (a NOA

Edited by Dr. Maya Ilieva (ASSOCIATE EDITOR) / Prof. Ramón Zúñiga (CO-EDITOR-IN-CHIEF).

Extended author information available on the last page of the article

Published online: 20 November 2023

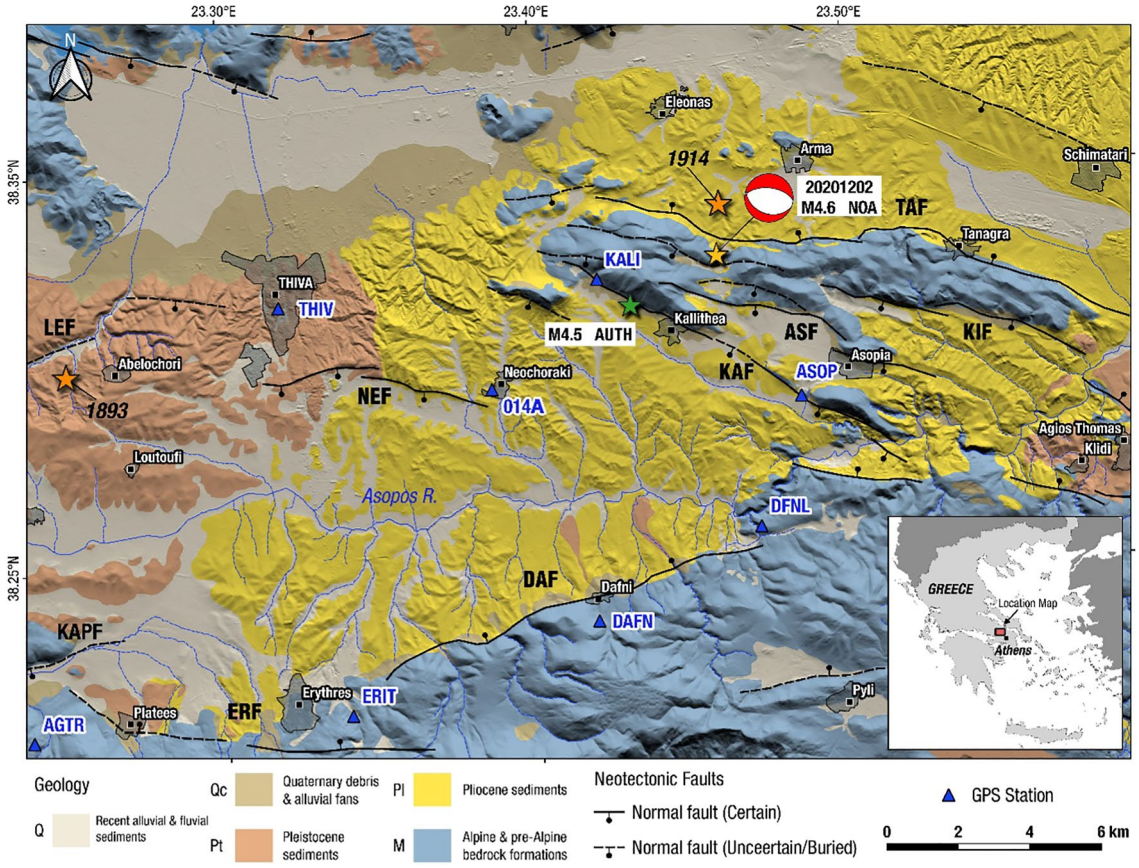

Fig. 1 Location map showing simplified geology, shaded relief, the focal mechanism (beachball; NOA solution) and the epicentre (yellow star) of the Kallithea 2 December 2020 earthquake. Triangles indicate GPS (GNSS) station locations of a local network (Ganas et al. 2007a). Orange stars indicate the locations of the 1893 and 1914 M6 epicentres. Black lines are active faults (NOAFAULTs database, Ganas 2022; Goldsworthy and Jackson 2001; Sboras et al. 2010). Fault names: KAPF (Kaparelli Fault), ERF (Erythres Fault), DAF (Dafni Fault), NEF (Neohoraki Fault), KAF (Kallithea Fault), ASF (Asopia Fault), TAF: (Tanagra fault), KIF (Kirikio Fault), LEF (Leontari Fault)

campaign station belonging to the KAPNET network; Ganas et al. 2007a; Marinou et al. 2015) in the vicinity of the epicentre (Fig. 1). Furthermore, the earthquake occurred within a region with a rich history of M6+ seismic events during the last two centuries (Ambraseys and Jackson 1990) where the NW–SE striking normal faults of the Gulf of Evia rift (Lemeille 1977; Rondoyanni-Tsiambaou 1984; Roberts and Jackson 1991; Ganas and White 1996; Ganas 1997; Kranis 1999; Ganas and Papoulia 2000; Goldsworthy and Jackson 2001; Sboras et al. 2006, 2010; Walker et al. 2010; Georgiou 2019) intersect (and vice-versa) the E–W striking normal faults of the Gulf of Corinth rift and its continuation towards southern Viotia (also written Beotia or Boeotia; Jackson et al. 1982; Papanikolaou et al. 1988; Stewart and Hancock 1991; Roberts and Koukouvelas 1996; Roberts and Ganas 2000; Ganas et al. 2005, 2007b; Kokkalas et al. 2007; Sakellariou et al. 2007; Tsodoulos et al. 2008).

Our research methods include the processing and analysis of geodetic (InSAR, GNSS) and seismological data. First, we present a detailed analysis of the geodetic data. The SAR images acquired by the SENTINEL-1 satellites are routinely distributed free of charge by the European Space Agency (ESA). The GNSS data originated from three sources: (a) from a permanent station west of the epicentre (station THIV) that was provided by the Greek private GNSS network HxGN SmartNet, (b) the permanent GNSS station 014A belonging to the national GNSS network of Greece HEPOS (https://www.hepos.gr/Map/SensorMap.aspx) and (c) the campaign GNSS station KALI that is part of the NOA local network KAPNET (Ganas et al. 2007a; Marinou et al. 2015). We then derive a co-seismic fault model from joint inversion of geodetic data (GNSS and InSAR) assuming that the earthquake can be modelled by the slip on a rectangular fault buried in an elastic and homogeneous half-space.

We also inferred kinematic source parameters by analysing waveforms recorded by the Hellenic Unified Seismological Network (HUSN) and the National Observatory of Athens Seismic Network. Our analysis aimed at the comparison

of the two datasets (geodetic vs. seismological) given the very shallow depth of the slip centroid, as reported by NOA (2020). An additional aspect of our research concerns the rupture pattern of the active NW–SE striking normal faults in Viotia,, which continue southwards in Attica (e.g., Ganas et al. 2005; Grützner et al. 2016; Deligiannakis et al. 2018; Iezzi et al. 2021), despite their intersection with the E–W normal faults of the Gulf of Corinth that have propagated in this area during Quaternary (e.g., Roberts and Ganas 2000; Tsodoulos et al. 2008). Is it possible that the South Viotia NW–SE faults rupture partially in moderate magnitude earthquakes or do they rupture as whole segments? Are the ruptures shallow or at mid crustal depths? Are the normal fault segments single structures or comprise fault zones with several branches down-dip (vertical segmentation; e.g., Childs et al. 1996)? The unique case of the Kallithea $M=4.6$ earthquake may shed light on some of those questions.

Tectonic setting: geology

Numerous structural studies have shown that central Greece is a young, extensional province of the Aegean area and one of the most actively deforming in the world (King et al. 1985; Roberts and Jackson 1991; Stewart and Hancock 1991; Collier et al. 1998; Roberts and Ganas 2000; Goldsworthy and Jackson 2001; Goldsworthy et al. 2002). Surface topography and geomorphology are clearly associated with seismic activity along large normal faults that have developed over the last 1–5 Ma (million years; Jackson et al. 1982; Roberts and Ganas 2000; Ganas et al. 2005, 2007b; Tsodoulos et al. 2008; Grützner et al. 2016; Deligiannakis et al. 2018; Iezzi et al. 2021). Extension is mainly directed N–S with increasing rates towards the west (Clarke et al. 1998; Briole et al. 2000; Avallone et al. 2004; Chousianitis et al. 2013; D'Agostino et al. 2020; Briole et al. 2021). The main extensional features are two E–W to NW–SE Pliocene–Pleistocene rifts, namely the Gulf of Corinth and the Gulf of Evia (Fig. 1; Ambraseys and Jackson 1990; Ganas and Papoulia 2000; Goldsworthy and Jackson 2001; Ganas et al. 2004, 2005; Walker et al. 2010; Fernández-Blanco et al. 2019). In between the two major rifts, there are smaller structures comprising mainly E–W striking active normal faults with mostly antithetic dip, i.e. to the south, that are capable of hosting events up to ~ M6.0 such as the 2013 Kallidromon Mountain sequence (Ganas et al. 2014) or have well-developed limestone scarps with thick colluvium on their hanging wall but with unknown post-glacial activity (e.g., Ganas et al. 2007b). Other significant normal faults are visible on the eastern margin of the Gulf of Corinth and along the Asopos river valley (Fig. 1; Papanikolaou et al. 1988; Ganas et al. 2005; Sboras et al. 2006, 2010; Tsodoulos et al. 2008). One such fault is the south-dipping Kaparelli fault that ruptured on 4 March 1981 (Jackson et al. 1982; Kokkalas et al. 2007). Another one is the Corini fault in south-west Viotia that is arranged en-echelon to the Kaparelli Fault and preliminary structural data were presented in Ganas et al., (2007b).

In the Thiva–Kallithea region (Fig. 1), Late Miocene–Pliocene normal faulting juxtaposed Upper Triassic–Jurassic carbonates, which were deposited in shallow-water environments onto syn-rift lacustrine-brackish deposits. Since at least Pliocene times, central Greece has been subjected to NE–SW (more recently N–S) oriented extension due to post-orogenic extension and back-arc stretching imposed by the African slab rollback (e.g., Jolivet and Brun 2010). At present, this extensional regime is mostly accommodated by seismic slip along active normal faults striking mainly WNW–ESE, which have been intersected by a younger generation of E–W faults, generating several Plio-Quaternary basins (e.g., Asopos, Thiva, Schimatari; Papanikolaou et al. 1988; Goldsworthy et al. 2002; Georgiou 2019; see Fig. 1 for locations). The 2020 event near Kallithea highlighted the structural complexity in this region of the Asopos Rift valley as the reactivation of the WNW–ESE structures indicates their significant role in strain accommodation and that they still represent a seismic hazard for this region.

Previous strong earthquake activity near Thiva includes the shallow events of 11 May 1893 and 17 October 1914 with magnitudes reaching or slightly exceeding 6.0 (Ambraseys and Jackson 1990; Kaviris et al. 2022; Fig. 1). Both events destroyed Thiva (intensities were assigned to 9 on the MSI scale). The damage reports of the 1914 event included villages to the east of Thiva such as Tanagra (Fig. 1) so the epicentre was located by Ambraseys and Jackson (1990) somewhere in between. Despite the M6.0 magnitudes, no surface ruptures were reported, either because of a lack of ground surveys or for the ruptures did not appear on the ground surface. A full account of past earthquakes near Thiva is given by Kaviris et al. (2022). The present-day stress field as determined by analyses of focal mechanism data is extensional (N–S) and is manifested by the orientation of the T (extensional) principal axis of the moment tensors being related to the S_3 minimum principal axis of the stress tensor (Kapetanidis and Kassaras 2019).

Seismicity

The $M_W=4.6$ earthquake of 2 December 2020 10:54 UTC occurred to the east of the city of Thiva (Fig. 1), along an ESE–WNW striking normal fault as indicated by the moment tensor solutions of regional data (NOA 2020; also compiled by EMSC; https://www.emsc-csem.org/; see also Elias et al. 2021; Kaviris et al. 2022). The mapped active structures in this area dip to the southwest (Goldsworthy

et al. 2002; Sboras et al. 2010; Ganas 2022); there are three normal faults NEF, KAF, ASF (Fig. 1) with lengths between 3 and 6 km, so it is reasonable to initially assume that one of these faults hosted the earthquake. We note that both Sboras et al. (2010) and Georgiou (2019) mapped two segments of the Kallithea fault, one abutting the homonymous village and a second segment, towards the SE, running along the "Mavrovouni" ridge (see the bedrock ridge above station ASOP in Fig. 1). The NOA epicentre (38.3272°N 23.4590°E) plots on the footwall of both KAF and ASF (about 3 km NE from Kallithea village), while the Aristotle University of Thessaloniki (AUTH; see the catalog at http://geophysics.geo.auth.gr/ss/CATALOGS/preliminary/finalcat.cat) AUTH epicentre location (38.315°N23.431°E; magnitude $M=4.5$) plots in the immediate hanging wall of KAF (Fig. 1).

Four focal mechanisms are available for the Kallithea event with fault strike determinations N106°E–N137°E, i.e., in broad agreement with geological data. Until 31 December 2020 more than 110 aftershocks (with $0.8 \leq M_L \leq 3.5$) were recorded by NOA (Fig. 2). The depth distribution of the aftershocks is notably shallower than background seismicity (NOA catalog data; Fig. 3) within a 20-km radius of Kallithea, indicating a shallow earthquake sequence. We also note that the moment tensor solutions of the mainshock (see Table 1) indicate shallow normal faulting (four out of five solutions indicate depths between 1 and 4 km). The

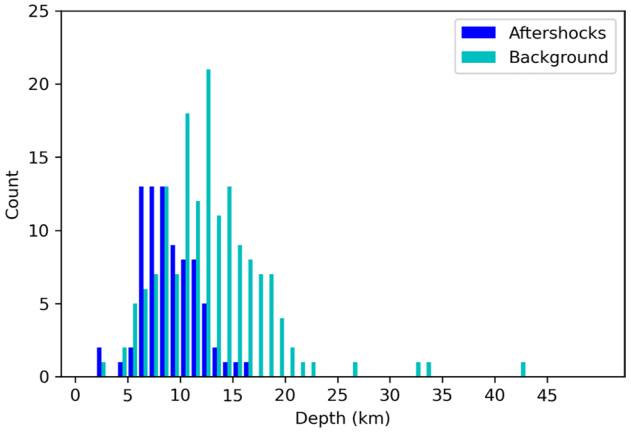

Fig. 3 Graph showing the frequency—focal depth distribution of earthquakes for the background period (1/1–1/12/2020; cyan colour) and for the Kallithea seismic sequence ($N=80$; 2/12/2020–24/12/2020; blue colour), respectively. Data source: NOA catalogue of revised events

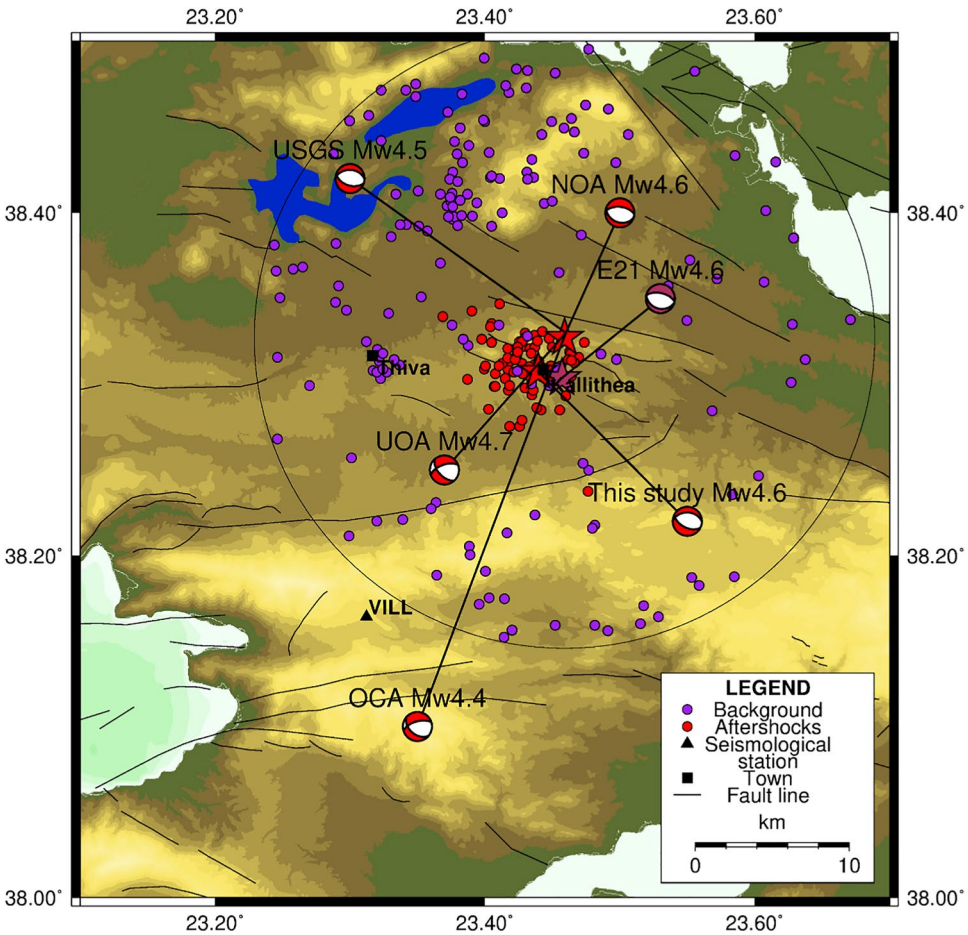

Fig. 2 Relief map showing earthquake epicentres in a 20-km area surrounding the 2 December 2020 event (red star) for the period 1 January 2020–1 December 2020 (data source NOA). Red circles indicate aftershock locations, violet circles background seismicity, respectively. Thin black lines are faults from Ganas (2022)

Table 1 List of focal mechanism (moment tensor) solutions of the mainshock determined by NOA (National Observatory of Athens), OCA (Géoazur), USGS (United States Geological Survey) UOA (University of Athens), Elias et al. (2021; row E21) and this study (inversion of geodetic data). Column depth indicates centroid depth

Agency	Time UTC	Lat (°)	Long (°)	Depth (km)	Magnitude M_w	Strike1 (°)	Dip1 (°)	Rake1 (°)	Strike2 (°)	Dip2 (°)	Rake2 (°)	M_O (N m)
NOA	10:54:56	38.2870	23.4580	1.6	4.6	108	46	−83	278	43	−97	7.71E+15
OCA	10:54:56	38.310	23.400	4.0	4.7	130	45	−43	253	61	−126	–
USGS	10:54:58	38.349	24.458	2.0	4.5	108	51	−80	272	40	−102	6.94E+15
UOA	10:54:56	38.3152	23.4439	12	4.7	137	56	−37	250	60	−140	1.61E+16
E21		38.3037	23.4572	1.0	4.6	106	31	−87				8.95E+15
This study		38.3073	23.4395	1.1	4.6	117	54	−74				1.42E+16

aftershock sequence extends within a radius of 5 km of the village of Kallithea with most of events occurring to the WSW of the mainshock (Fig. 2). Elias et al. (2021) relocated the seismicity data and presented an aftershock distribution mostly to the southwest of Kallithea and deeper than the centroid of the mainshock (aftershock depths between 2 and 5 km) without a down-dip alignment. As the location accuracy of the seismological solutions may reach up to a few kilometres, we also used additional geodetic data analysis in order to map the surface displacement field and better locate the seismic fault and its relationship to the Kallithea normal fault. An additional point of concern is the dip-angle of the seismic fault, i.e., a low angle as suggested by Elias et al. (2021) or a moderate–high angle as indicated by the focal mechanisms in Table 1.

Geodetic data and methods

Sentinel-1 interferograms

We produced co-seismic interferograms using Sentinel-1 radar imagery for both the ascending (track 102) and the descending (track 007) orbits. The two pairs of SAR acquisitions were processed with the SNAP v8.0 ESA software (https://step.esa.int). For both tracks, the pre-event and post-event acquisitions are on 27 November 2020 and on 3 December 2020, respectively. The interferograms were produced by complex multiplication of the primary (pre-event) image with the complex conjugate of the secondary (post-event) image. The phase of such a complex image (interferogram) is related to the ground displacement between the two images. The obtained interferograms are shown in Fig. 4a and b; in both cases, we observed about two fringes each (coloured from blue to red) corresponding to a motion away from the satellite. Since the LOS displacement has a similar amplitude and pattern in both ascending and descending tracks, we can conclude that a vertical ground motion is predominant.

Phase unwrapping was carried out by using SNAPHU (Chen and Zebker 2002). We then applied a decomposition procedure to the ascending and descending unwrapped interferograms (Wright et al. 2004) in order to obtain the vertical displacement map shown in Fig. 4c. We found that 7 cm of subsidence occurred in the hanging-wall of the Kallithea normal fault, which can be interpreted as the result of a co-seismic motion along either (a) the Kallithea normal fault itself, running ESE–WNW and dipping to the south (fault code GR0608 in the NOAFAULTs database; Ganas 2022) or (b) along a 'blind' normal fault, parallel and synthetic to the Kallithea Fault whose geometry is unknown. This hypothesis will be investigated by geodetic inversion modelling in "Fault model" section.

In summary, the InSAR data fit the overall neotectonic pattern of the broader Thiva region as the epicentral area is characterised by an extensional structural setting, with fault structures trending approximately NW–SE (Fig. 4b) dipping either towards southwest or towards northeast. However, coseismic deformation has only been detected in the region of the village of Kallithea where it trends about N115°E (Fig. 4c; see also Elias et al. 2021, their Fig. 6). The surface deformation derived from the interferometric measurements (acquired along ascending and descending orbits) reveals a "spoon-like" geometry, elongated in the NW–SE direction, compatible to the orientation and south dip-direction of the Kallithea fault (or to a fault sub-parallel and synthetic to Kallithea F.), with an extent of about 8 km^2.

Co-seismic motion of the GNSS stations

We analysed the daily data files (dual-frequency observations at 30-s sampling interval) of two permanent GNSS stations, station THIV belonging to the HxGN SmartNet and the station 014A belonging to the HEPOS Greek state network. Both stations are located to the west of the epicentre (Fig. 1). Station 014A is located about 5 km from the village of Kallithea (the location with the highest macroseismic intensity; see Fig. S1). The processing was done using the GIPSY—Precise

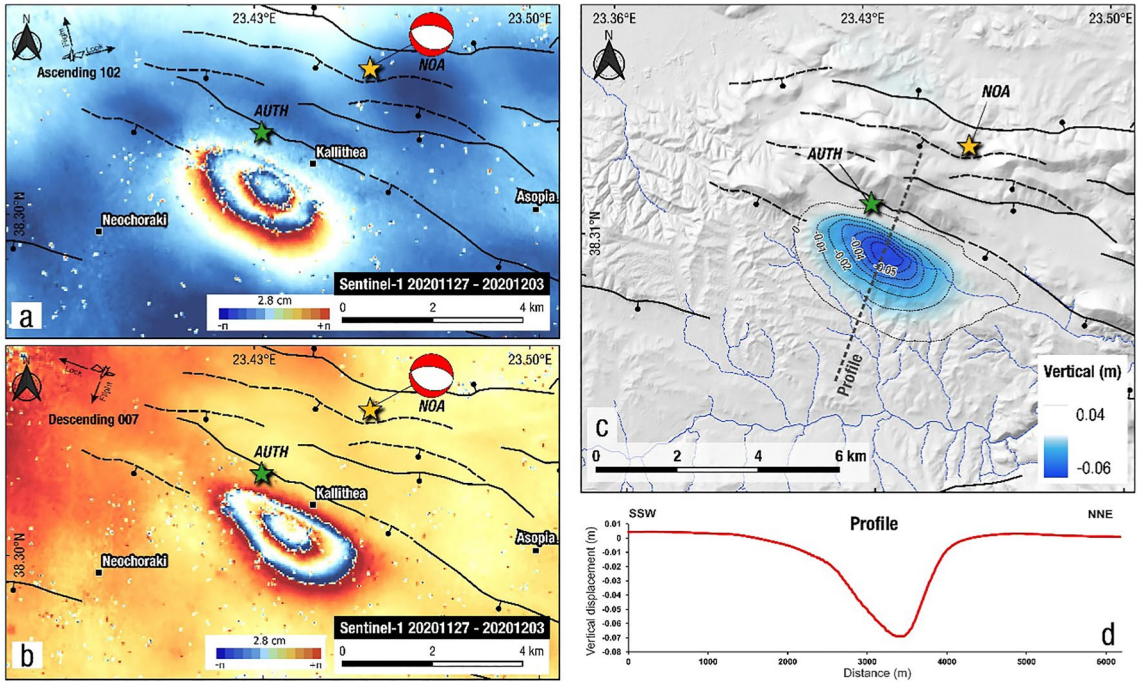

Fig. 4 The co-seismic interferograms (wrapped phase; cropped swath; unwrapped) over the Kallithea area. One cycle of colour corresponds to 28 mm of displacement along the line of sight. **a** Wrapped phase showing the ascending image pair, **b** wrapped phase showing the descending image pair, **c** vertical displacement obtained by decomposing the ascending and descending data and showing co-seismic subsidence with WNW–ESE orientation, **d** cross-section orthogonal to fault's strike showing vertical displacement in m (see profile trace in c)

Point Positioning (PPP) software and Fig. 5a, b shows the time series of the two stations. At THIV the position time series is 10-year long and stable. With this quality of data, the threshold of detectability is around 1 mm, therefore GNSS certifies that the displacement at this location is below this value (a similar result was obtained by Elias et al. 2021). On 16 December 2020, we also re-occupied a GNSS benchmark of the KAPNET local network (station KALI; Ganas et al. 2007a; Marinou et al. 2015) which is located about 2 km to the northwest of Kallithea (Fig. 1). Figure 5c shows the time series of coordinates from station KALI, detrended for a secular velocity that we assumed to be the same as THIV. We did not see any offset in the time series providing evidence of a co-seismic deformation, so this observation provides a useful constraint on the zero displacement on the InSAR displacement field. The GNSS data confirmed that the ground displacements at the three sites were very small, below noise level of the measurement so they were not used in the geodetic model inversion.

Fault model

We jointly modelled the line-of-sight (LOS) displacement field retrieved from both ascending and descending InSAR data with a finite dislocation fault in an elastic and homogeneous half-space (Okada 1992) with a typical Poisson's ratio value of 0.25. We also applied a topography compensation (to relate the source depth to the actual ground surface) and assessed possible residual offsets and ramps in the InSAR measurements. Moreover, the InSAR data were preliminarily down-sampled to a 70-m regular grid in order to reduce the computational load of the inversion process.

Our source modelling strategy is based on a well-established two-step approach capable of computing the distribution of co-seismic slip over the fault plane (Atzori et al. 2008, 2009; Atzori and Salvi 2014); in particular, we use the implementation of the ENVI SARscape® software. The first step is carried out by fitting a uniform slip model to the data (via a nonlinear inversion) to constrain the geometry of the fault plane; in particular, it provides the position of one point of the plane and the values of strike and dip angles. This step also computes the uniform slip value (and its rake) and the fault plane dimensions (length and width). However, these parameters are refined in the second step; in fact, we compute (via a linear inversion; see Fig. 6) the slip distribution over the inferred fault plane by partitioning it into a number of small patches. The distribution of the patches with a non-zero slip value finally defines the extension of the actual slipping part of the plane (rupture area).

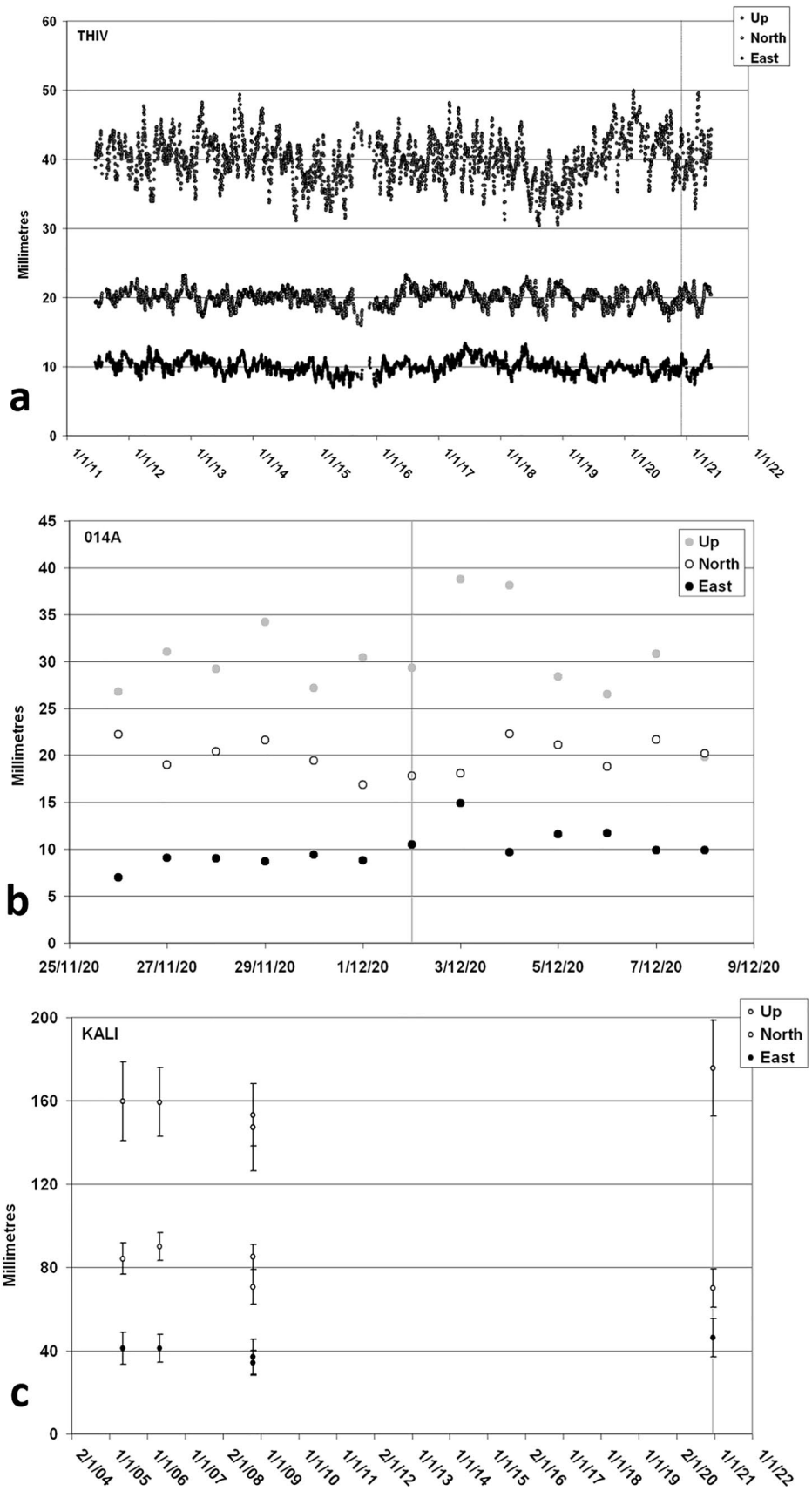

Fig. 5 Position time series (E, N, Up) of GNSS station THIV (**a**) 014A (**b**) and campaign KALI (**c**); see location in Fig. 1. The thin grey line indicates the time of the main shock. The deformation signal is not large enough to be separated from the measurement error (noise)

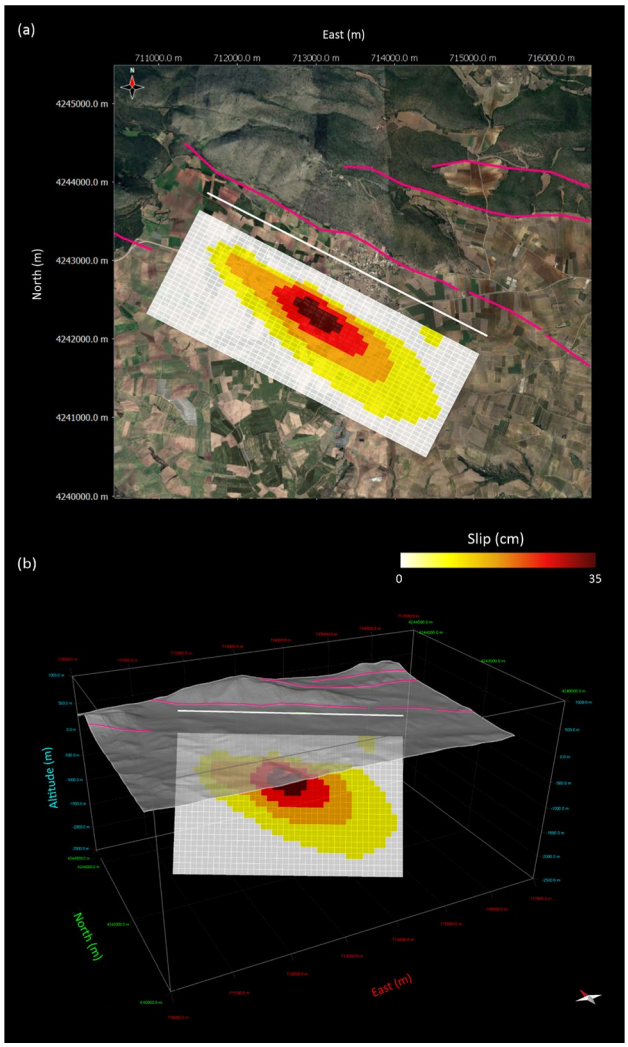

Fig. 6 Map (top) and 3-D view of the coseismic slip distribution of the Kallithea earthquake rupture**.** The retrieved model parameters are listed in Table 2. The distributed slip over a mesh of 100×100 m^2 is displayed as a projection in a map view (top panel) and in 3D view (bottom panel)

Based on this approach, we performed the preliminary uniform slip modelling without constraints; our best solution is characterised by one fault plane oriented N117.2E° and dipping 53.8° southwest (see the parametric analysis of uncertainties in Fig. S2). Note that these values are consistent with the moment tensor solution found by USGS and NOA (see Table 1). The retrieved parameters highlighted a normal faulting mechanism with a slight strike-slip component (left-lateral). Our nonlinear model (for uniform slip) shows that the slipped area corresponds to a plane with an area of 2.1×0.7 km^2 that does not reach the ground surface (depth to top fault is 795 m below ground surface). In order to calculate the slip distribution by using a linear inversion, we considered patches of 100×100 m^2 covering a plane that includes the previously computed uniform slip fault. The final slip distribution over the modelled fault plane is shown in Fig. 6 in map view (top) and 3D view (bottom). We suggest that the maximum slip value is 0.35 m, which is reached at a depth of about 1100 m. Moreover, assuming a value of 0.01 m as the threshold for non-slipping areas—chosen according to the uncertainty resolution of the available data—we measured an actual slipped area of about 4.6×10^6 m^2 or about three times the size of the modelled uniform slip fault plane. The retrieved slip distribution is centered on the area of maximum slip but it is elongated in the direction NW–SE, i.e., parallel to the fault's strike with a deepening towards SE.

In Fig. 7, we present the comparison between the observed geodetic (InSAR) data and the LOS-projected modelled results (non-uniform slip model) for both ascending (first row) and descending (second row) orbits. The first and second columns show the maps (data and models), respectively, while the third column presents their difference (residuals). It can be seen that the retrieved source parameters are able to reproduce the observed signal with excellent approximation, since the residuals are less than 1.5 cm, with large areas showing even much lower values.

All the retrieved fault parameters are summarised in Table 2. We also note that the retrieved seismic source has a geodetic moment of 1.42×10^{16} Nm, corresponding to a moment magnitude of 4.7, which is fairly consistent with the value estimated by the NOA MT ($M_W = 4.6$).

Kinematic source parameters, seismic energy and radiation efficiency

We collected waveforms recorded at 54 stations managed by the Hellenic Seismological Network (HUSN) and by the National Observatory of Athens Seismic Network (see Acknowledgments section for network details). Based on the maximum epicentral distance—set to 230 km—and the signal-to-noise ratio (SNR), we inferred source parameters at the 15 stations indicated with blue triangles in Fig. S4.

Spectral modelling

We removed the instrumental response and bandpass filtered the original waveforms in the range 0.1–20 Hz by using a 4 poles Butterworth filter. We picked the S phase (on the three components) and used a variable time window to select the signal portion to be inverted. The windowed signal is then tapered with a cosine taper function. We applied the multitaper approach (Prieto et al. 2009) to obtain the amplitude velocity spectra. This approach has been proven to reduce the leakage effect (Prieto et al. 2009). The velocity spectra are then converted into displacement spectra by integration

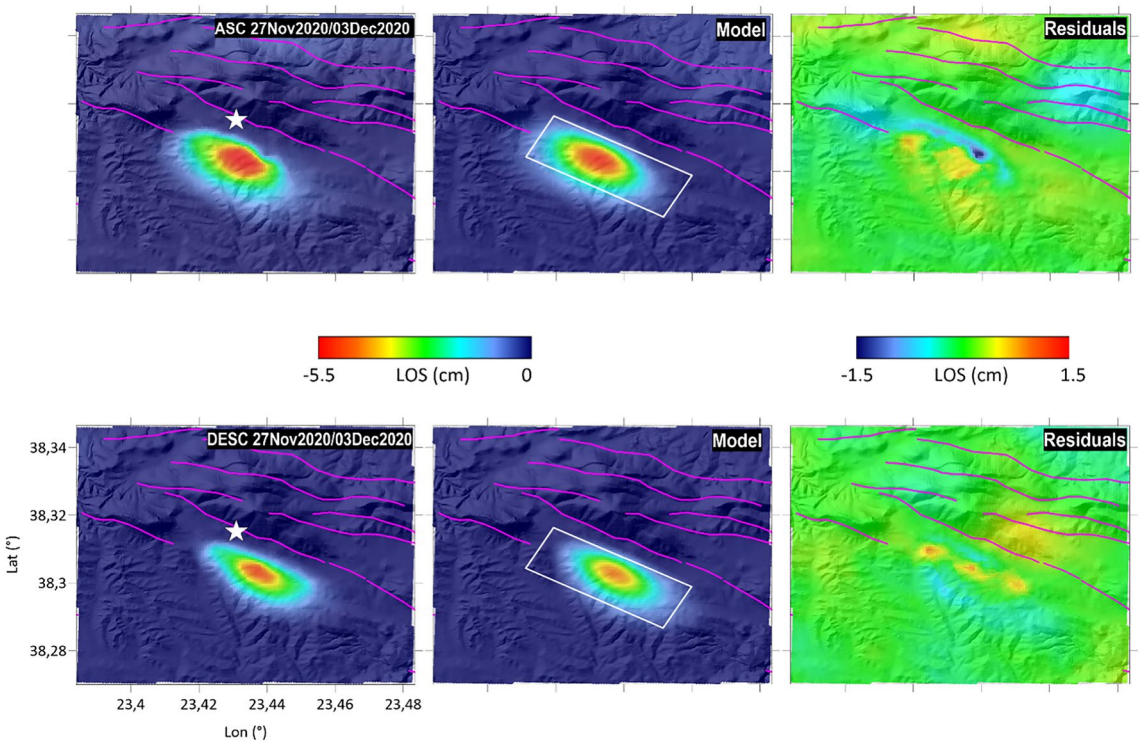

Fig. 7 Maps showing the modelling of the InSAR data: Left) Data, Middle) modelling results, and left) residuals for ascending (ASC) and descending (DESC) orbits of InSAR interferograms. The middle panel shows Line of sight (LOS) projected displacement maps computed from the retrieved analytical model for the Sentinel-1 interferograms. The outline of the retrieved rupture plane is indicated by the white rectangle, while the magenta lines represent the mapped faults of the area retrieved from the NOAFaults v4.0 database (Ganas 2022). The white star indicates the epicentre (AUTH) of the main shock. Uniform slip modelling results are presented in Fig. S3 in the Supplementary Material

Table 2 List of parameters of the seismic fault from linear inversion of the geodetic data

Parameter	This study	Elias et al. (2021)
Moment magnitude (geodetic)	4.7	
Geodetic moment [Nm]	1.42×10^{16}	1.6×10^{16}
Centre of top-fault LON [deg]	23.437541	23.4378
Centre of top-fault LAT [deg]	38.304468	38.3051
Azimuth—strike [deg]	N117.2 E	N120E (locked)
Depth of top fault edge* [m]	795	700
Depth of the max slip [m]	1100	1100
Length* [m]	2100	2000
Width* [m]	718	1300
Rupture area** [m^2]	4.6 10^6	
Dip [deg]	53.8	48 (locked)
Rake [deg]	−74.0	−74
Maximum slip [m]	0.31	
Mean slip [m]	0.11	0.24

*Estimated from nonlinear inversion (uniform slip model)

**Summing up the area of all the slipped patches from the non-uniform slip model

in the frequency domain. The final spectrum is obtained from the vector composition of the three components.

We adopted the Boatwright spectral model (Boatwright 1980) in order to estimate the spectral level at low frequency Ω_0, the corner frequency (f_c) and the quality factor (Q):

$$\Omega(f) = \frac{\Omega_0 e^{-\frac{\pi f T}{Q}}}{\left[1 + \left(\frac{f}{f_c}\right)^{\gamma}\right]^{\frac{1}{2}}}, \quad (1)$$

where f is the frequency, T is the travel time of the seismic phase considered, the exponential function takes into account for the anelastic attenuation, while the parameter γ controlling the spectral decay at high frequency is assumed to be equal to 4. Note also that for the anelastic attenuation, we have assumed a frequency independent quality factor Q.

Following Zollo et al. (2014), we applied the approach of Ben-Menahem and Singh (1981) to account for the geometrical spreading. To this aim, we used the crustal model of Ganas et al. (2014) to compute the take-off angle for each station.

To infer the model parameters, a spectral fitting was implemented via a grid search approach. A weight is

assigned to each spectral point depending on the logarithm of the SNR. The noise corresponds to the pre-P noise computed on the vertical component. In a first step, we obtained a preliminary estimate of Ω_0 by fitting only the flat part of the displacement spectrum. Using the best-fit value Ω_0^{best}, we then inverted for the other two parameters, i.e., f_c and Q. We also refine the estimate of Ω_0 by exploring the range $\Omega_0^{\text{best}} \pm \sigma_{\Omega_0}$ obtained in the first step.

To illustrate the results of this modelling procedure, we show in Fig. 8 four examples of observed and computed displacement spectra at stations indicated in each panel, whose locations are given in Fig. S4 and whose corresponding waveforms are shown in Fig. S5 to S8. Furthermore, we computed the average values of those inferred parameters at each station. By using the inferred Ω_0, we obtained $M_0 = 1.06 \times 10^{16}$ (7.63×10^{15}, 1.47×10^{16}) N m, which corresponds to $M_W = 4.6$ (4.5, 4.7), while we obtained $f_c = 1.35$ (1.05, 1.73) Hz and $Q = 371 \pm 94$.

Kinematic source parameters

From the selected model and the obtained model parameters, we computed the static stress drop using the Brune's (1970) model as $\Delta\sigma = 0.44 M_0 / r^3$, where r is the *source radius*. For a circular source model, this latter can be obtained from the corner frequency ($r = 0.37 v_s / f_c$, where v_S is the S-wave velocity, assumed here as 3228 m/s and corresponding to the mean value between the velocity at the source and that at the receiver). Similarly, we computed the mean slip as $\Delta u = M_0 / \mu \pi r^2$, where μ is the shear modulus assumed here as 3.3×10^{10} Pa.

We obtained $r = 1414$ (1102, 1813) m, $\Delta\sigma = 11.3$ (4.8,26.8) MPa and $\Delta u = 0.16$ (0.08, 0.30) m. For all the considered parameters, the uncertainties, corresponding to the 95% confidence intervals, have been computed by using the technique proposed by Prieto et al. (2007). It is worth noting that the value of M_0 and the mean slip are in agreement with the results obtained from the geodetic data inversion modelling (reported in Table 2).

Seismic energy and radiation efficiency

Seismic energy (E_S) is measured from the integral of the square of the ground motion velocity computed in the frequency domain, *Ic* (Boatwright and Fletcher 1984):

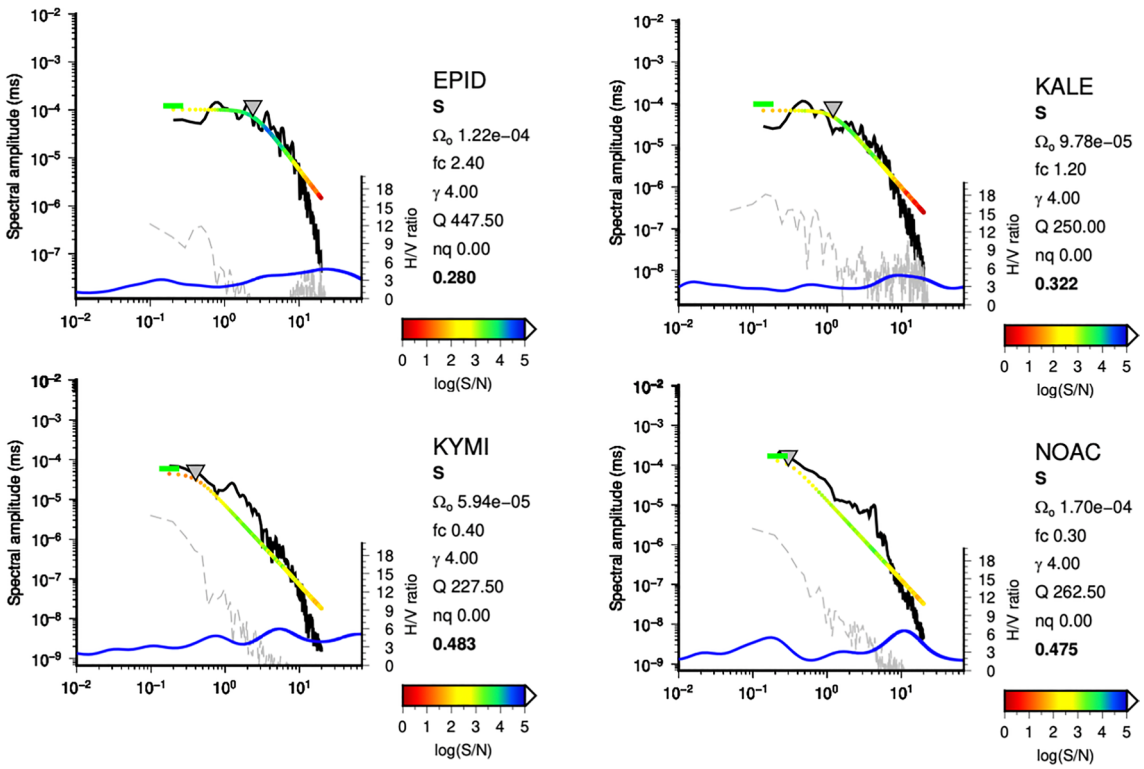

Fig. 8 Observed (black lines) and modelled (coloured lines) displacement spectra at four stations. The modelled spectra are colour coded according to the logarithm of the SNR. The locations of the stations are given in Fig. S4 while corresponding waveforms are shown in Fig. S5 to S8. The grey dashed line represents the pre-P noise selected on the vertical component. The blue line corresponds to the *H*/*V* spectral ratio. For each station the best-fit parameters are also reported together with the final misfit, which is shown in bold

$$E_s = \frac{4\pi\rho v_S R^2}{F^2} I_c = \frac{4\pi\rho v_S R^2}{F^2} \frac{1}{\pi} \int_0^\infty \omega^2 |U(\omega)|^2 d\omega, \quad (2)$$

where R is the hypocentral distance, ρ the density and F is the free surface coefficient. We computed the displacement spectrum $U(\omega)$ from the previously obtained best-fitting spectral model (Zollo et al. 2014) corrected for the frequency band limitation (e.g., Ide and Beroza 2001). Then, the seismic energy is used to compute the apparent stress $\tau_a = \mu E_s/\mathrm{Mo}$ (Wyss and Molnar 1972) where μ is the crustal shear modulus (3.3×10^{10} Pa), and the radiation efficiency as $\eta_{SW} = \tau_a/\Delta\sigma$. We obtained $E_S = 1.81$ (0.62, 5.28) 10^{12} J, $\tau_a = 4.24$ (1.78, 10.11) MPa and $\eta_{SW} = 0.375$.

In order to obtain a model independent estimate of η_{SW}, we computed the total energy E_T (by neglecting the thermal energy). We used the obtained value for the radiated energy E_s while calculating total fracture energy E_G from the stress drop map. For this purpose, we converted slip to stress using the approach proposed by Ripperger and Mai (2004). Specifically, the slip map obtained from the geodetic modelling is transformed into the 2D wavenumber ($\boldsymbol{k}$) domain and multiplied by the static stiffness function $K(\boldsymbol{k})$ in the same domain to obtain the 2D transform $\Delta\sigma(\boldsymbol{k})$ of the stress drop. Finally, $\Delta\sigma(\boldsymbol{k})$ is transformed in the along strike, along dip space to map the static stress drop on the fault plane.

The $\Delta\sigma$—distribution result is shown in fault-plane view (Fig. 9) and indicates that the maximum stress drop is about 25 MPa, and there is also a stress increase in the upper right (SE) part of the fault-slip map where future events may occur.

The same technique allowed us to compute the specific energy $E_{SG} = 2.3 \times 10^5$ J/m^2. Selecting as the actual slipped fault area 4.61×10^6 m^2 (obtained by considering only slip values greater than 0.01 m), the mean stress drop value obtained from the map is 4.5 MPa, which corresponds to the lower limit of the values obtained from the spectral inversion. The fracture energy is $E_G = 1.11 \times 10^{12}$ J, providing a total energy $Es + E_G$, of 2.92×10^{12} J and a radiation efficiency $\eta = (E_R/(E_R + E_G))$ of 0.62. This result suggests that most of the available energy was radiated during the earthquake. Thus, in addition to the shallow depth, the high efficiency of the earthquake may have contributed to the disproportional observed effects (damage to Kallithea village) compared to the relatively moderate magnitude.

Discussion

Surface deformation and earthquake magnitude (M4.6)

Very shallow earthquakes can induce ground deformation even at magnitudes as low as $M_W = 4.1$ (case of the 14 April 2019 event in Utah; Mesimeri et al. 2021). The mainshock of the 2020 Kallithea sequence is another case of a very shallow earthquake with moderate magnitude. In fact, it is the first time in Greece that InSAR has imaged surface deformation associated with a $M_W = 4.6$ earthquake. We suggest that this is due to the shallow depth of the maximum slip (1.1 km) as provided by the inversion of the geodetic data

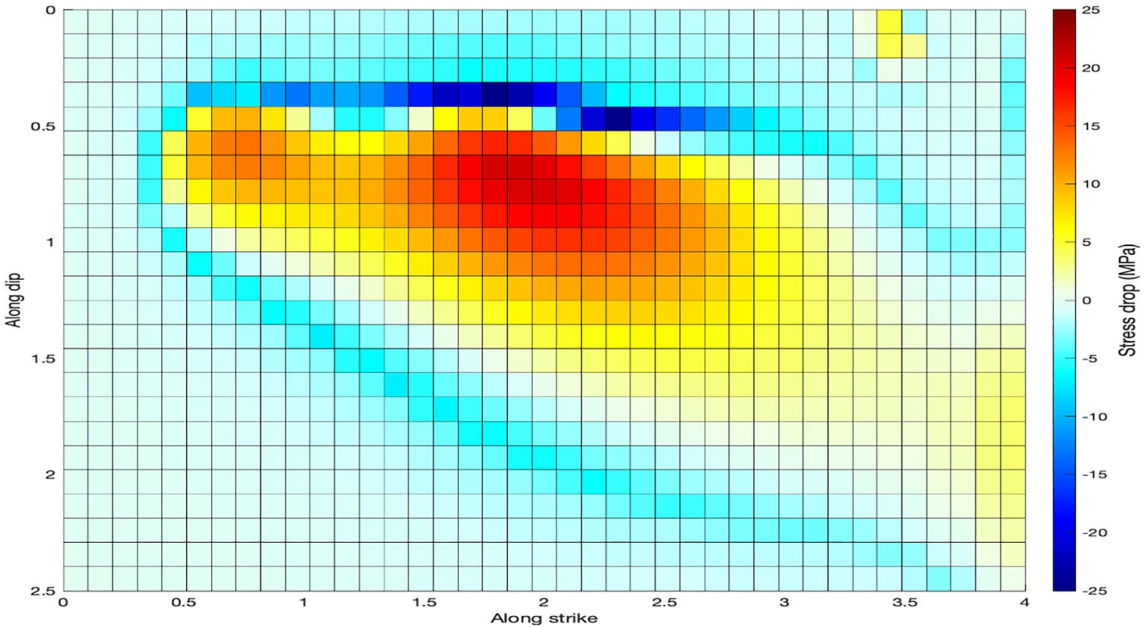

Fig. 9 Static stress drop map in MPa obtained from the distributed slip map

(Fig. 6). We also mapped an asymmetric pattern of surface displacements across the Kallithea normal fault, i.e., the deformation was mapped entirely on the hanging wall of the Kallithea Fault (Fig. 4). The maximum hanging wall subsidence is estimated at 7 cm (on the decomposed vertical component). The strike-parallel pattern of surface deformation (Fig. 4c) also showed that the deformation resulting from co-seismic motion along the south-dipping normal fault confirms a strong relationship with present-day topography, as the maximum co-seismic subsidence correlates with topographic lows. The depth to the top of the fault is about 800 m (Table 2), indicating that either this fault is a young "blind" structure accommodating crustal extension or the 2020 event was a partial rupture of the Kallithea normal fault that did not reach the ground surface.

This case is interesting in view of very shallow earthquakes that occur from time to time in various places around the world (e.g., Messinia 2011 swarm, Kyriakopoulos et al. 2013; Niger 2017 event, Craig and Gibbons 2022; Le Teil 2019, De Novellis et al. 2020; Sparta earthquake in the eastern US, Figueiredo et al. 2022; the 2007 events in western Australia, Dawson et al. 2008), including places that are supposed to have low seismicity because of low strain rates, such as Le Teil in south France. The occurrence of such shallow earthquakes might be accelerated by human activity (Le Teil), but this does not seem to be the case for Kallithea even though there is industry activity (quarrying) located about 6 km to the NE of the Kallithea fault (i.e., in its footwall). In fact, this activity is not located in the very near field of the fault, which could have played a role assuming a mechanism of normal stress reduction, leading to unclamping (unlocking) of the fault plane.

It is also interesting to examine whether very shallow events are associated with particular conditions of ground water level. Groundwater level changes may increase the pore pressure along the fault plane, thereby facilitating slip. For Kallithea, Kaviris et al. (2022) examined rainfall patterns in relation to the ground deformation time series of station THIV (vertical component) and found a good correlation. It should be noted that rainfall patterns may reflect on seasonal trends in groundwater level, which induces a small-scale (a few cm) of seasonal variations in GNSS data (see also Argyrakis et al. 2020), therefore its use as a proxy may be justified in cases where there are no data from boreholes or wells in the vicinity of earthquakes.

Unfortunately, no water level data are available in the vicinity of Kallithea, making it difficult to prove a link to this earthquake using the GNSS vertical component time series as a proxy. In any case, we do not observe changes more than ± 1.5 cm on the vertical component of the two GNSS stations during the last 9 years preceding the earthquake (THIV and 014A; Fig. 5). In addition, using optical remote sensing (Sentinel-2 data), we have not detected any significant changes in land-use in recent years that could reflect a potential impact of groundwater loading and unloading effects. There may be a yet unknown deep source of fluids that could circulate along the Kallithea fault plane and reached the 2020 rupture plane, but we have no data to support this hypothesis. A seismic swarm that occurred about 10 km west of Kallithea during 2021 (July to October) was associated with deep fluids (Kaviris et al. 2022) but the depth range of these events was between 8 and 12 km. Therefore, we are inclined to suggest that the 2020 Kallithea earthquake resulted from regular tectonic loading since the seismic fault is located close (5–7 km; Fig. 1) to a crustal block boundary (a site of strain localisation) in central Greece, the E–W Asopos rift, bridging the Quaternary rifts of Corinth and South Gulf of Evia (Reilinger et al. 2006; Marinou et al. 2015; Briole et al. 2021; see Fig. S9 for a structural cross-section).

Comparison of fault parameters derived from spectral modelling of seismological data and the geodetic modelling

An interesting result of our study is the similarity of the main kinematic parameters independently obtained by the InSAR data modelling and seismic waveforms analysis (with consistent elastic parameters), as can be seen from the comparison of Tables 2 and 3. In particular, the estimates of moment magnitude and mean slip values are consistent; this suggests the occurrence of a rather simple rupture process involving a single fault and a smooth slip distribution, which is reasonable for a $M_W = 4.6$ magnitude event. Also, the rupture area (RA) values are similar, and are consistent with the Wells and Coppersmith (1994) relationships which, for an event size of $M_W = 4.6$ and a normal fault mechanism, provide RA $= 7.9 \pm 3.3$ km^2. The consistency of the two mean slip values may also suggest that almost

Table 3 Source of the kinematic source parameters inferred from the spectral inversion. The numbers in parenthesis correspond to the 95% confidence interval

Seismic moment [Nm]	1.06×10^{16} (7.63×10^{15}, 1.47×10^{16})
Moment magnitude	4.6 (4.5, 4.7)
Corner frequency [Hz]	1.35 (1.05, 1.73)
Source radius [m[	1414 (1102, 1813)
Rupture area [km^2]	6.3 (3.8, 10.3)
Stress drop [MPa]	11.3 (4.8, 26.8)
Mean slip [m]	0.16 (0.08, 0.30)
Seismic energy [J]	1.81 (0.62, 5.28) 10^{12}
Apparent stress [MPa]	4.24(1.78, 10.11)
Radiation efficiency	0.375 (0.371, 0.377)

all the accumulated strain energy was released during the earthquake. This result is indeed confirmed by the relatively high value of the radiation efficiency $\eta = 0.62$. Moreover, the high radiation efficiency and high stress drop (mean value of about 11 MPa) could have contributed to the disproportionate effects observed (damages to Kallithea village) compared to the relatively moderate magnitude.

Origin of shallow rupture

As noted above, the Kallithea earthquake that occurred at very shallow depth and, despite its moderate magnitude, produced noticeable surface deformation. This is not unusual as similar effects have been observed for other events such as the 1986 Mw = 5.2 Cusco earthquake, the 2010 Mw = 5.0 Pisayambo earthquake occurred in Ecuadorian Andes (Champenois et al. 2017), the 2017 Mw = 3.9 Ischia earthquake in Italy (De Novellis et al. 2018; Calderoni et al. 2019), the 2019 Mw = 4.9 Le Teil earthquake in France (e.g., De Novellis et al. 2020) and the 2018 M5.3 Lake Muir earthquakes in western Australia (Clark et al. 2020).

Only for two of the five earthquakes mentioned above stress drop estimates are available. In particular, for the Ischia earthquake Calderoni et al. (2019) have found a stress drop value of 0.01 MPa, while for the Le Teil earthquake De Novellis et al. (2020) reported a stress drop value of 1.3 MPa. These values are significantly lower than the 11.3 MPa inferred for the Kallithea earthquake, which may indicate some difference between these earthquakes.

A common feature characterising those events is the fact that the slip is concentrated in the upper part of the fault. For the 2010 Mw = 5.0 Pisayambo earthquake, Champenois et al. (2017) ascribed this result to a low rigidity medium. A similar argument has been proposed by Ritz et al. (2020) for the Le Teil earthquake. In both studies, a low rigidity value was also used to reconcile the seismic moment estimate obtained from InSAR data and seismological data. However, for the case of the Kallithea earthquake, the seismic moments inferred from the DInSAR data and from seismological data are very consistent, so a low rigidity medium is not a necessary condition.

We propose here two additional arguments that may help to explain the shallow location of the slip. The first one is that there may be a structural barrier at 1.5–2 km depth due to an intersection with a neighbouring fault, such as the known Kallithea fault (Fig. 10) that did not allow the rupture to propagate deeper. This scenario is possible assuming a 54° dip for the 2020 normal fault and a ~ 45° dip for the Kallithea fault (Fig. 10) but our capability of resolving between the two faults is at the limit of the accuracy of the method and data available. The second point relates to the limited energy budget available for the rupture propagation. Specifically, as reported in the previous section, we estimated a specific energy value of $E_{SG} = 2.3\ 10^5$ J/m^2. Assuming a linear slip-weakening model and a zero value for the strength excess (i.e., the initial stress is equal to the yielding stress), we can compute the characteristic slip-weakening distance (Dc) over which the energy is dissipated. Indeed, by using the previous assumption, the fracture energy is $E_{SG} = ½\ \Delta\sigma \cdot Dc$ (Andrews 1976; Guatteri and Spudich 2000) providing a Dc value of 0.04 m, which is a consistent with the expected value for a $M_W = 4.6$ event (Ohnaka 2000; Colombelli et al. 2014). Such critical slip distance corresponds to a critical size of the nucleation zone Lc ($= \mu\ Dc / \Delta\sigma$) of about 117 m. Thus, according to the nucleation model proposed by Ohnaka (2000) the rupture of such a small patch can lead to a small earthquake that prevents the rupture of the deeper and probably stronger fault plane.

Rupture plane and segmentation pattern around Kallithea

We further explore the location of our modelled fault (see its surface projection in Fig. 10; rectangle in green colour) and discuss its relationship with the known structures in the area, such as the Kallithea fault (KAF in Fig. 1). We can do that through the analysis of a cross-section A–A′ orthogonal to the strike of both faults (Fig. 10). This shows that our modelled fault and the Kallithea fault are almost parallel and synthetic in terms of kinematics. However, their traces are separated,, by an across-strike distance of about 905 m (Fig. 10; distance between points T and F, i.e. between the line where the projection of our model top-fault plane reaches the surface and the Kallithea fault trace) However, in terms of top-fault depth this distance reduces to 430 m so it is within the expected position uncertainty of the inversion modelling (see error bars in cross-section of Fig. 10 and see Fig. S2 east & north uncertainties), thus making it difficult to declare whether these two faults are separated or coincident.

In order to gain more insights into this point, we re-modelled the InSAR data by performing a linear inversion after constraining all the geometric parameters (position, strike and dip) to be those of the Kallithea fault, using a dip-angle scenario of 60°. The obtained results (see Table S1 and Fig. S10 in Supplementary Material) show that, although the modelled slip is reasonably concentrated around a region at the centre of the fault plane, the corresponding ground displacement fits the InSAR data very poorly. This allows us to conclude that either the observed displacement could be attributed to a new, previously unknown fault different from the Kallithea fault, or the modelling of the Kallithea fault parameters (for example the dip-angle of 60°) needs to be updated.

With the data and modelling currently available, the question of the activated fault plane remains open and certainly worthy of further investigation. In the following, we present

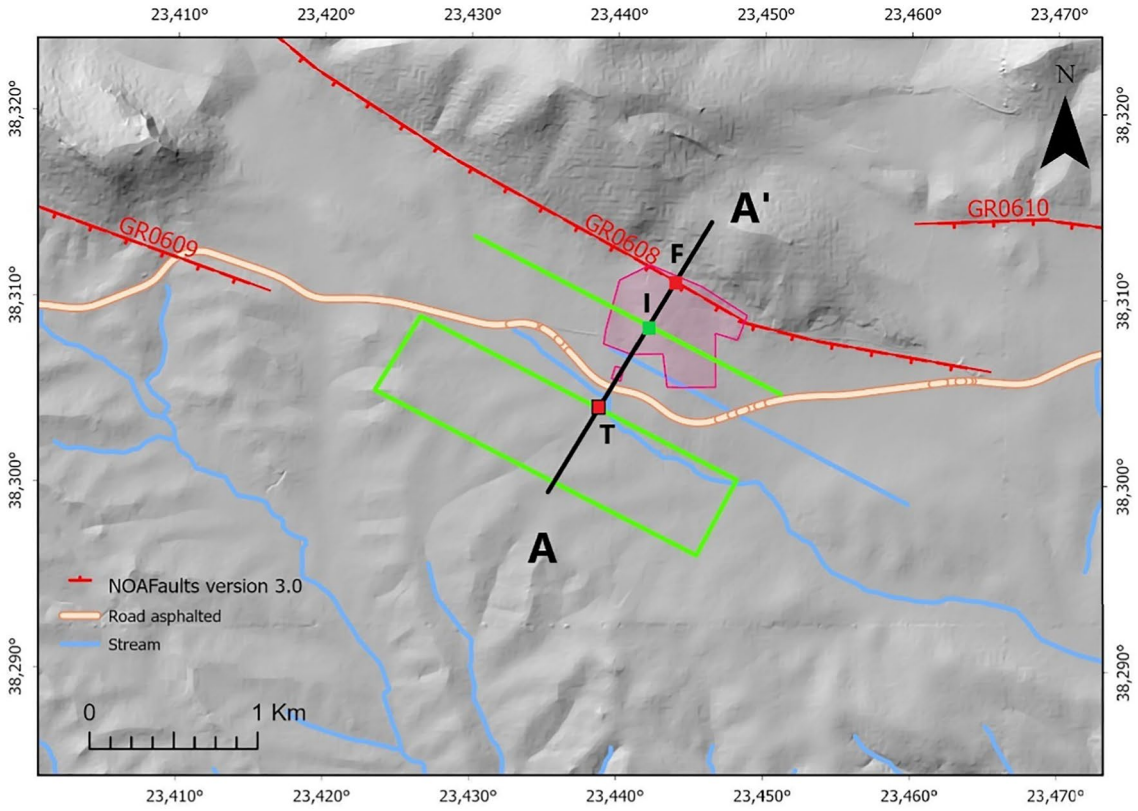
23,410°
23,420°
23,430°
23,440°
23,450°
23,460°
23,470°
38,320°
38,310°
38,300°
38,290°
N
A'
A
F
I
T
GR0608
GR0609
GR0610
NOAFaults version 3.0
Road asphalted
Stream
0
1 Km

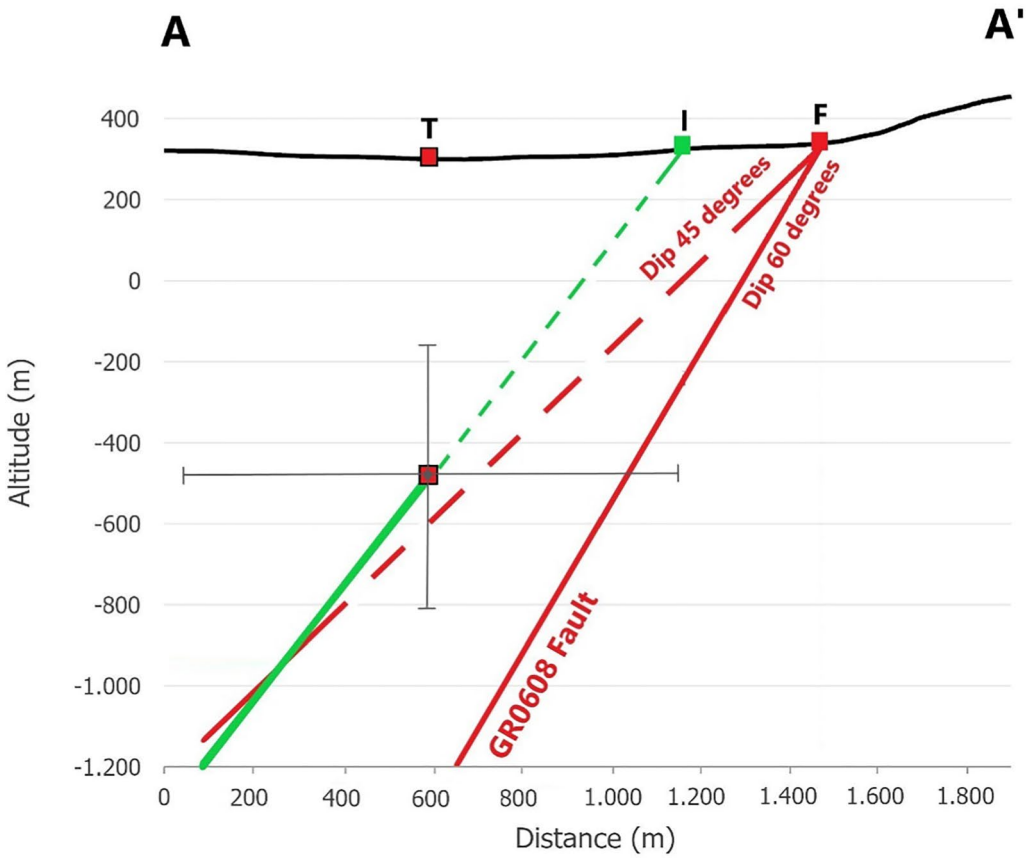
A
A'
T
I
F
400
200
0
-200
-400
-600
-800
-1.000
-1.200
Altitude (m)
Dip 45 degrees
Dip 60 degrees
GR0608 Fault
0
200
400
600
800
1.000
1.200
1.400
1.600
1.800
Distance (m)

◂**Fig. 10** Relief map (top) and cross-section (bottom) depicting normal fault planes near village Kallithea. The cross section is shown by a thin black line on the map. The green plane is the 2020 modelled seismic fault, the red plane is the Kallithea SW-dipping fault (continuous line is with 60° dip; dashed line is with 45° dip)

some speculative reasoning on the implication of the presence of a newly identified fault.

In terms of dip-angle, Georgiou (2019) reports field measurements for the Kallithea fault between 44° and 52°, so it is geometrically doable that the possible new fault joins the Kallithea one at the depth range of ~ 950–1500 m (Fig. 10). If this is the case, then the 2020 rupture plane may branch off the Kallithea fault. In an alternative scenario, the two faults run parallel until the depth of ~ 1500 m when the 2020 rupture stops. Without more data we cannot exclude either scenario although the kinematic arguments presented in "Origin of shallow rupture" section seem to favor the branching one. On a smaller (local) scale such a fault architecture resembles the "step-up" structures of Stewart and Hancock (1991); however, given that the fault tip is found at a depth of 795 m (under Neogene deposits), it is not possible to observe vertical fractures due to "shattering" (Stewart and Hancock 1990). We note that the size of the 2020 rupture (roughly 2.1 by 0.71 km; according to the results of the nonlinear inversion) and its location would be indicative of a hanging wall migration process and abandoning of the neotectonic Kallithea fault (Goldsworthy and Jackson 2001; Ganas et al. 2004; Palyvos et al. 2005). Another possible explanation could be that the normal fault (Kallithea proper) found on the footwall of the 2020 seismic fault (red line in Fig. 10) is also active, but it is now sharing accumulated strain release with the new fault. The tectonic strain may now accumulate faster on this new, synthetic structure which is of Late Quaternary age and it comprises a single segment.

In the pre-InSAR era, an earthquake of M4.6 near the village of Kallithea would almost certainly be assigned to the Kallithea south-dipping normal fault. With the use of InSAR data and modelling, we end up that this is not necessarily the case and, as such, it offers a structural clue on the accommodation of strain inside young, cross-cutting rifts. The use of the geodetic data and modelling call for a possible presence of two different fault planes that keep separated at least up to a depth of about 950 m (Fig. 10); however, due to the close proximity of the two fault traces (Fig. 10; Kallithea fault and the 2020 rupture plane), and the uncertainties involved in geodetic data inversion there is a possibility that a gentler Kallithea fault geometry may be able to fit the data. In that case, the Kallithea fault ruptured in an unusual way in the sense that it released only part of the accumulated energy without rupturing its entire length (6 km). More data are necessary to resolve the geometry of the active structures near Kallithea such as high-resolution fault zone observations (e.g., Karastathis et al. 2007; Pucci et al. 2016; Porras et al. 2022).

Conclusions

1. We used Sentinel-1 interferograms to map ground deformation due to the $M_w = 4.6$ December 2, 2020 shallow earthquake near Thiva (central Greece). Because of the shallow depth of the main event and the good coherence of the radar signals, the ground subsidence (which has a maximum value of 7 cm) is well visible with InSAR.
2. Using dislocation modelling, we identified that the seismic fault is striking N117°E, has a dip angle of ~ 54° towards the south, its rupture area is roughly 4.6 km^2, it slipped by a maximum amount of 0.31 m with a slip centroid depth of 1.1 km.
3. Whether this fault is separated from or coincident to the well-known neotectonic Kallithea normal fault remains debated due to the accuracy limitations associated with the inversion model and data used; however, forward modelling obtained by fixing a high-angle Kallithea fault geometry fails to fit the data, thus indicating that either there is a new (undetected) normal fault south of the Kallithea fault, or the Kallithea fault parameters need to be investigated using high-resolution techniques.
4. A third possible interpretation is that the two normal faults are separated and merge at depths ~ 950–1500 m, so that the 2020 fault plane branches off the Kallithea fault.
5. The geodetically based model results are in agreement with the source parameters obtained by the analysis of broadband seismological data.
6. The earthquake was characterised by a radiation efficiency $\eta = 0.62$, which indicates that most of the available energy was radiated during the earthquake contributing to the disproportional observed effects compared to the relatively moderate magnitude.
7. Our study confirmed that, also in Greece, moderate ($4.5 \leq Mw \leq 4.7$) shallow events can be traced in InSAR studies and can produce surface displacements useful for fault modelling.
8. The 2020 shallow event near Kallithea highlighted the structural complexity in this region of the Asopos Rift valley as the reactivation of the WNW–ESE structures indicates their significant role in strain accommodation and that they still represent a seismic hazard for this region of central Greece.

Supplementary Information The online version contains supplementary material available at https://doi.org/10.1007/s11600-023-01213-2.

Acknowledgements We thank one anonymous reviewer and Dr Letizia Anderlini (INGV) for their constructive reviews. We also thank Efthimios Sokos, Panagiotis Elias, Zafeiria Roumelioti, Aggeliki Marinou, George Kaviris, Stelios Bitharis, Marinos Charalampakis and Vasilis Kapetanidis for comments and discussions. We acknowledge Vasilis Kapetanidis for his help with retrieving the response files of the seismic sensors. Athanassios Ganas thanks "HELPOS—Hellenic Plate Observing System" (MIS 5002697) which was funded by the Operational Programme "Competitiveness, Entrepreneurship and Innovation" (NSRF 2014-2020) and co-financed by Greece and the European Union (European Regional Development Fund). V.C. was supported by Pianeta Dinamico – Working Earth INGV-MUR Project. We are indebted to ESA for making available the satellite images for free. GNSS permanent station data were provided by Hexagon SmartNET and Ktimatologio SA. We used data from the following seismic networks, HL (Institute of Geodynamics, National Observatory of Athens, https://doi.org/10.7914/SN/HL), HP (University of Patras, https://doi.org/10.7914/SN/HP), HT (Aristotle University of Thessaloniki, https://doi.org/10.7914/SN/HT), HA (National and Kapodistrian University of Athens, https://doi.org/10.7914/SN/HA), and HI Institute of Engineering Seismology and Earthquake Engineering, https://doi.org/10.7914/SN/HI) networks. Some figures were made with open-source software GMT (Wessel et al. 2013). The publication of the article in OA mode was financially supported by HEAL-Link.

Funding Open access funding provided by HEAL-Link Greece.

Declarations

Conflict of interest On behalf of all authors, the corresponding author states that there is no conflict of interest.

References

Ambraseys NN, Jackson JA (1990) Seismicity and associated strain of central Greece between 1890 and 1988. Geophys J Int 101(3):663–708

Andrews DJ (1976) Rupture propagation with finite stress in antiplane strain. J Geophys Res 81:3575–3582

Argyrakis P, Ganas A, Valkaniotis S et al (2020) Anthropogenically induced subsidence in Thessaly, central Greece: new evidence from GNSS data. Nat Hazards 102:179–200. https://doi.org/10.1007/s11069-020-03917-w

Atzori S, Salvi S (2014) SAR data analysis in solid earth geophysics: from science to risk management. In: Holecz F, Pasquali P, Milisavljevic N, Closson D (eds) Land applications of radar remote sensing. Intech Open, London. https://doi.org/10.5772/57479

Atzori S, Manunta M, Fornaro G, Ganas A, Salvi S (2008) Postseismic displacement of the 1999 Athens earthquake retrieved by the differential interferometry by synthetic aperture radar time series. J Geophys Res-Solid Earth 113:B09309. https://doi.org/10.1029/2007JB005504

Atzori S, Hunstad I, Chini M, Salvi S, Tolomei C, Bignami C, Stramondo S, Trasatti E, Antonioli A, Boschi E (2009) Finite fault inversion of DInSAR coseismic displacement of the 2009 L'Aquila earthquake (central Italy). Geophys Res Lett 36:L15305

Avallone A, Briole P, Agatza-Balodimou AM, Billiris H, Charade O, Mitsakaki C, Nercessian A et al (2004) Analysis of eleven years of deformation measured by GPS in the Corinth Rift Laboratory area. C R Geosci 336(4–5):301–311

Ben-Menahem A, Singh SJ (1981) Seismic waves and sources. Springer, New York

Boatwright J (1980) A spectral theory for circular seismic sources: simple estimates of source dimension, dynamic stress drop, and radiated seismic energy. Bull Seismol Soc Am 70:1–28

Boatwright J, Fletcher JB (1984) The partition of radiated energy between P and S waves. Bull Seismol Soc Am 74:361–376

Briole P, Rigo A, Lyon-Caen H et al (2000) Active deformation of the Corinth rift, Greece: results from repeated global positioning system surveys between 1990 and 1995. J Geophys Res 105(B11):25605–25625

Briole P, Ganas A, Elias P, Dimitrov D (2021) The GPS velocity field of the Aegean. New observations, contribution of the earthquakes, crustal blocks model. Geophys J Int. https://doi.org/10.1093/gji/ggab089

Brune JN (1970) Tectonic stress and the spectra of seismic shear waves from earthquakes. J Geophys Res 75:4997–5009

Calderoni G, Di Giovambattista R, Pezzo G, Albano M, Atzori S, Tolomei C, Ventura G (2019) Seismic and geodetic evidences of a hydrothermal source in the Md 4.0 2017, Ischia earthquake (Italy). J Geophys Res Solid Earth 124:5014–5029. https://doi.org/10.1029/2018JB016431

Champenois J, Baize S, Vallee M, Jomard H, Alvarado A, Espin P, Ekström G, Audin L (2017) Evidences of surface rupture associated with a low-magnitude (Mw5.0) shallow earthquake in the Ecuadorian Andes. J Geophys Res Solid Earth 2017:122

Chen CW, Zebker HA (2002) Phase unwrapping for large SAR interferograms: statistical segmentation and generalized network models. IEEE Trans Geosci Remote Sens 40:1709–1719

Childs C, Nicol A, Walsh JJ, Watterson J (1996) Growth of vertically segmented normal faults. J Struct Geol 18(12):1389–1397. https://doi.org/10.1016/S0191-8141(96)00060-0

Chousianitis K, Ganas A, Gianniou M (2013) Kinematic interpretation of present-day crustal deformation in central Greece from continuous GPS measurements. J Geodyn 71:1–13

Clark DJ, Brennand S, Brenn G, Garthwaite MC, Dimech J, Allen TI, Standen S (2020) Surface deformation relating to the 2018 Lake Muir earthquake sequence, southwest Western Australia: new insight into stable continental region earthquakes. Solid Earth 11:691–717. https://doi.org/10.5194/se-11-691-2020

Clarke PJ, Davies RR, England PC et al (1998) Crustal strain in central Greece from repeated GPS measurements in the interval 1989–1997. Geophys J Int 135(1):195–214

Collier REL, Pantosti D, D'Addezio G, De Martini PM, Masana E, Sakellariou D (1998) Paleoseismicity of the 1981 Corinth earthquake fault: Seismic contribution to extensional strain in central Greece and implications for seismic hazard. J Geophys Res 103(B12):30001–30019. https://doi.org/10.1029/98JB02643

Colombelli S, Zollo A, Festa G et al (2014) Evidence for a difference in rupture initiation between small and large earthquakes. Nat Commun 5:3958. https://doi.org/10.1038/ncomms4958

Craig TJ, Gibbons SJ (2022) Resolving the location of small intracontinental earthquakes using Open Access seismic and geodetic data: lessons from the 2017 January 18 mb 4.3, Ténéré, Niger,

earthquake. Geophys J Int 230(3):1775–1787. https://doi.org/10.1093/gji/ggac144
D'Agostino N, Métois M, Koci R, Duni L, Kuka N, Ganas A, Georgiev I, Jouanne F, Kaludjerovic N, Kandić R (2020) Active crustal deformation and rotations in the southwestern Balkans from continuous GPS measurements. Earth Planet Sci Lett 539:116246. https://doi.org/10.1016/j.epsl.2020.116246
Dawson J, Cummins P, Tregoning P, Leonard M (2008) Shallow intraplate earthquakes in Western Australia observed by interferometric synthetic aperture radar. J Geophys Res Solid Earth 113(B11):B11408. https://doi.org/10.1029/2008JB005807
De Novellis V, Carlino S, Castaldo R, Tramelli A, De Luca C, Pino NA et al (2018) The 21 August 2017 Ischia (Italy) earthquake source model inferred from seismological, GPS, and DInSAR measurements. Geophys Res Lett 45(5):2193–2202
De Novellis V, Convertito V, Valkaniotis S et al (2020) Coincident locations of rupture nucleation during the 2019 Le Teil earthquake, France and maximum stress change from local cement quarrying. Commun Earth Environ 1:20. https://doi.org/10.1038/s43247-020-00021-6
Deligiannakis G, Papanikolaou ID, Roberts G (2018) Fault specific GIS based seismic hazard maps for the Attica region, Greece. Geomorphology 306:264–282. https://doi.org/10.1016/j.geomorph.2016.12.005
Elias P, Spingos I, Kaviris G, Karavias A, Gatsios T, Sakkas V, Parcharidis I (2021) Combined geodetic and seismological study of the December 2020 Mw = 4.6 Thiva (Central Greece) shallow earthquake. Appl Sci 11:5947. https://doi.org/10.3390/app11135947
Fernández-Blanco D, de Gelder G, Lacassin R, Armijo R (2019) A new crustal fault formed the modern Corinth Rift. Earth Sci Rev 199:102919. https://doi.org/10.1016/j.earscirev.2019.102919
Figueiredo P, Hill J, Merschat A, Scheip C, Stewart K, Owen L, Wooten R, Carter M, Szymanski E, Horton S, Wegmann K, Bohnenstiehl D, Thompson G, Witt A, Cattanach B, Douglas T (2022) The Mw 5.1, 9 August 2020, Sparta earthquake, North Carolina: the first documented seismic surface rupture in the eastern United States. Geol Soc Am. https://doi.org/10.17615/z077-0z17
Ganas A, Papoulia I (2000) High-resolution, digital mapping of the seismic hazard within the Gulf of Evia Rift, Central Greece using normal fault segments as line sources. Nat Hazards 22(3):203–223
Ganas A, White K (1996) Neotectonic fault segments and footwall geomorphology in Eastern Central Greece from Landsat TM data. Geol Soc Greece Sp Pubi 6:169–175
Ganas A, Pavlides SB, Sboras S, Valkaniotis S, Papaioannou S, Alexandris AG, Plessa A, Papadopoulos GA (2004) Active fault geometry and kinematics in Parnitha Mountain, Attica. Greece J Struct Geol 26:2103–2118
Ganas A, Pavlides S, Karastathis V (2005) DEM-based morphometry of range-front escarpments in Attica, central Greece, and its relation to fault slip rates. Geomorphology 65:301–319
Ganas A, Bosy J, Petro L, Drakatos G, Kontny B, Stercz M, Melis NS, Cacon S, Kiratzi A (2007a) Monitoring active structures in eastern Corinth Gulf (Greece): the Kaparelli fault. Acta Geodynamica Et Geomaterialia 4(1):67–75
Ganas A, Spina V, Alexandropoulou N, Oikonomou A, Drakatos G (2007b) The Corini active fault in south-western Viotia region, central Greece: segmentation, stress analysis and extensional strain patterns. Bull Geol Soc Greece 40:297–308. https://doi.org/10.12681/bgsg.16561
Ganas A, Karastathis V, Moshou A, Valkaniotis S, Mouzakiotis E, Papathanassiou G (2014) Aftershock relocation and frequency–size distribution, stress inversion and seismotectonic setting of the 7 August 2013 M=5.4 earthquake in Kallidromon Mountain, central Greece. Tectonophysics 617:101–113. https://doi.org/10.1016/j.tecto.2014.01.022
Ganas A (1997) Fault segmentation and seismic hazard assessment in the Gulf of Evia Rift, central Greece. Unpublished Ph.D. thesis, University of Reading, November 1997. http://ethos.bl.uk/OrderDetails.do?uin=uk.bl.ethos.363718
Ganas A (2022) NOAFAULTS KMZ layer Version 4.0 (V4.0). Zenodo. https://doi.org/10.5281/zenodo.6326260
Georgiou Ch (2019) Multiparametric investigation of faults in Eastern Central Greece. Ph.D. thesis (in Greek), National Technical University of Athens
Gianniou M (2010) Tectonic deformations in Greece and the operation of HEPOS network. In: EUREF 2010 symposium, June 2–4, Sweden
Goldsworthy M, Jackson J (2001) Migration of activity within normal fault systems: examples from the Quaternary of mainland Greece. J Struct Geol 23(2–3):489–506
Goldsworthy M, Jackson J, Haines J (2002) The continuity of active fault systems in Greece. Geophys J Int 148(3):596–618
Grützner C et al (2016) New constraints on extensional tectonics and seismic hazard in northern Attica, Greece: the case of the Milesi Fault. Geophys J Int 204(1):180–199. https://doi.org/10.1093/gji/ggv443
Guatteri M, Spudich P (2000) What can strong-motion data tell us about slip-weakening fault-friction laws? Bull Seismol Soc Am 90:98–116
Ide S, Beroza GC (2001) Does apparent stress vary with earthquake size? Geophys Res Lett 28:3349–3352
Iezzi F, Roberts G, Faure Walker J, Papanikolaou I, Ganas A et al (2021) Temporal and spatial earthquake clustering revealed through comparison of millennial strain-rates from 36Cl cosmogenic exposure dating and decadal GPS strain-rate. Sci Rep 11:23320. https://doi.org/10.1038/s41598-021-02131-3
Jackson JA, Gagnepain J et al (1982) Seismicity, normal faulting and the geomorphological development of the Gulf of Corinth (Greece): the Corinth earthquakes of February and March 1981. Earth Planet Sci Lett 57:377–397
Jolivet L, Brun JP (2010) Cenozoic geodynamic evolution of the Aegean region. Int J Earth Sci 99:109–138. https://doi.org/10.1007/s00531-008-0366-4
Kapetanidis V, Kassaras I (2019) Contemporary crustal stress of the Greek region deduced from earthquake focal mechanisms. J Geodyn 123:55–82. https://doi.org/10.1016/j.jog.2018.11.004
Karastathis VK, Ganas A, Makris J, Papoulia J, Dafnis P, Gerolymatou E, Drakatos G (2007) The application of shallow seismic techniques in the study of active faults: the Atalanti normal fault, central Greece. J Appl Geophys 62(3):215–233
Kaviris G, Kapetanidis V, Spingos I, Sakellariou N, Karakonstantis A, Kouskouna V, Elias P, Karavias A, Sakkas V, Gatsios T, Kassaras I, Alexopoulos JD, Papadimitriou P, Voulgaris N, Parcharidis I (2022) Investigation of the Thiva 2020–2021 earthquake sequence using seismological data and space techniques. Appl Sci 12(5):2630. https://doi.org/10.3390/app12052630
King GCP, Ouyang ZX, Papadimitriou P et al (1985) The evolution of the Gulf of Corinth (Greece)—an aftershock study of the 1981 earthquakes. Geophys J R Astron Soc 80(3):677
Kokkalas S, Pavlides S, Koukouvelas I, Ganas A, Stamatopoulos L (2007) Paleoseismicity of the Kaparelli fault (eastern Corinth Gulf): evidence for earthquake recurrence and fault behaviour. Boll Soc Geol Ital 126(2):387–395
Kranis HD (1999) Neotectonic activity of fault zones in central-eastern Mainland Greece (Lokris). Ph.D. thesis. GAIA, 10, 2003, 234pp
Kyriakopoulos Ch, Chini M, Bignami Ch, Stramondo S, Ganas A, Kolligri M, Moshou A (2013) Monthly migration of a tectonic

seismic swarm detected by DInSAR: southwest Peloponnese, Greece. Geophys J Int 194:1302–1309. https://doi.org/10.1093/gji/ggt196

Lemeille F (1977) Études néotectoniques en Grèce centrale nord-orientale (Eubée centrale, Attique, Béotie, Locride) et dans les Sporades du Nord. Thèse, Univ. Paris XI

Marinou A, Ganas A, Papazissi K, Paradissis D (2015) Strain patterns along the Kaparelli–Asopos rift (central Greece) from campaign GPS data. Ann Geophys 58(2):S0219

Mesimeri M, Pankow KL, Barnhart WD, Whidden KM, Hale JM (2021) Unusual seismic signals in the Sevier Desert, Utah possibly related to the Black Rock volcanic field. Geophys Res Lett 48:e2020GL090949. https://doi.org/10.1029/2020GL090949

NOA (2020) Moment tensor solution. https://bbnet.gein.noa.gr/gisola/realtime/2020/noa2020xqwbq/2021-06-26T01:35:53.415841Z/output/index.html

Ohnaka MA (2000) Physical scaling relation between the size of an earthquake and its nucleation zone size. Pure Appl Geophys 15:2259–2282

Okada Y (1992) Internal deformation due to shear and tensile faults in a half-space. Bull Seismol Soc Am 82:1018–1040

Palyvos N, Pantosti D, de Martini PM, Lemeille F, Sorel D et al (2005) The Aigion-Neos Erineos coastal normal fault system (western Corinth Gulf Rift, Greece): geomorphological signature, recent earthquake history, and evolution. J Geophys Res 110(B09302):1–15

Papanikolaou DJ, Mariolakos ID, Lekkas EL, Lozios SG (1988) Morphotectonic observations on the Asopos Basin and the coastal zone of Oropos. Contribution to the neotectonics of Northern Attica. Bull Geol Soc Greece 20(1):251–267

Porras D, Carrasco J, Carrasco P, González PJ (2022) Imaging extensional fault systems using deep electrical resistivity tomography: a case study of the Baza fault, Betic Cordillera, Spain. J Appl Geophys 202:104673. https://doi.org/10.1016/j.jappgeo.2022.104673

Prieto GA, Thomson DJ, Vernon FL, Shearer PM, Parker RL (2007) Confidence intervals for earthquake source parameters. Geophys J Int 168(3):1227–1234. https://doi.org/10.1111/j.1365-246X.2006.03257.x

Prieto GA, Parker RL, Vernon FL (2009) A Fortran 90 library for multitaper spectrum analysis. Comput Geosci 35:1701–1710. https://doi.org/10.1016/j.cageo.2008.06.007

Pucci S et al (2016) Deep electrical resistivity tomography along the tectonically active Middle Aterno Valley (2009 L'Aquila earthquake area, central Italy). Geophys J Int 207(2):967–982. https://doi.org/10.1093/gji/ggw308

Reilinger R et al (2006) GPS constraints on continental deformation in the Africa-Arabia-Eurasia continental collision zone and implications for the dynamics of plate interactions. J Geophys Res 111:B05411. https://doi.org/10.1029/2005JB004051

Ripperger J, Mai PM (2004) Fast computation of static stress changes on 2D faults from final slip distributions. Geophys Res Lett 31:L18610. https://doi.org/10.1029/2004GL020594

Ritz JF, Baize S, Ferry M et al (2020) Surface rupture and shallow fault reactivation during the 2019 Mw 4.9 Le Teil earthquake, France. Commun Earth Environ 1:10. https://doi.org/10.1038/s43247-020-0012-z

Roberts GP, Ganas A (2000) Fault-slip directions in central and southern Greece measured from striated and corrugated fault planes: comparison with focal mechanism and geodetic data. J Geophys Res 105(B10):23443–23462

Roberts S, Jackson JA (1991) Active normal faulting in central Greece: an overview. In: Roberts AM, Yielding G, Freeman B (eds) The geometry of normal faults, vol 56. Special Publications Geological Society of London, London, pp 125–142

Roberts GP, Koukouvelas I (1996) Structural and seismological segmentation of the Gulf of Corinth fault system: implications for models of fault growth. Ann Geofis 39:3

Rondoyanni-Tsiambaou Th (1984) Etude néotectonique des rivages occidentaux du canal d'Atalanti (Grèce centrale). Thèse 3e cycle, 190 pp. Univ. Paris-Sud, Orsay, France

Sakellariou D, Lykousis V, Alexandri S, Kaberi H, Rousakis G, Nomikou P, Georgiou P, Ballas D (2007) Faulting, seismic-stratigraphic architecture and Late Quaternary evolution of the Gulf of Alkyonides Basin-East Gulf of Corinth, Central Greece. Basin Res 19:273–295. https://doi.org/10.1111/j.1365-2117.2007.00322.x

Sboras S, Ganas A, Pavlides S (2010) Morphotectonic analysis of the neotectonic and active faults of Beotia (central Greece), using GIS techniques. Bull Geol Soc Greece 43(3):1607–1618. https://doi.org/10.12681/bgsg.11335

Sboras S, Ganas A, Pavlides S (2006) Tectonic geomorphology and active tectonics of the Asopos Rift valley, central Greece. In: 11th international symposium on natural and human induced hazards & 2nd workshop on earthquake prediction abstract volume, June 22–25, 2006, Patras, Greece, p 95

Stewart IS, Hancock PL (1990) Brecciation and fracturing within neotectonic normal fault zones in the Aegean region. In: Knipe RJ, Rutter EH (eds) Deformation mechanisms, rheology and tectonics, vol 54. Geological Society Special Publication, London, pp 105–110

Stewart IS, Hancock PL (1991) Scales of structural heterogeneity within neotectonic normal fault zones in the Aegean region. J Struct Geol 13:191–204. https://doi.org/10.1016/0191-8141(91)90066-R

Tsodoulos IM, Koukouvelas IK, Pavlides S (2008) Tectonic geomorphology of the easternmost extension of the Gulf of Corinth (Beotia, Central Greece). Tectonophysics 453(1–4):211–232. https://doi.org/10.1016/j.tecto.2007.06.015

Valkaniotis S, Ganas A (2020) Surface deformation observed in moderate Greek quake. Temblor. https://doi.org/10.32858/temblor.143

Walker RT, Claisse S, Telfer M, Nissen E, England P, Bryant CL, Bailey R (2010) Preliminary estimate of Holocene slip rate on active normal faults bounding the southern coast of the Gulf of Evia, central Greece. Geosphere 6(5):583–593

Wells DL, Coppersmith KJ (1994) New empirical relationships among magnitude, rupture length, rupture width, rupture area, and surface displacement. Bull Seismol Soc Am 84:974–1002

Wessel P, Smith WHF, Scharroo R, Luis J, Wobbe F (2013) Generic mapping tools: improved version released. EOS Trans AGU 94(45):409–410. https://doi.org/10.1002/2013EO450001

Wright TJ, Parsons BE, Lu Z (2004) Toward mapping surface deformation in three dimensions using InSAR. Geophys Res Lett 31:L01607. https://doi.org/10.1029/2003GL018827

Wyss M, Molnar P (1972) Efficiency, stress drop, apparent stress, effective stress, and frictional stress of Denver, Colorado, earthquakes. J Geophys Res 77(8):1433–1438. https://doi.org/10.1029/JB077i008p01433

Zollo A, Orefice A, Convertito V (2014) Source parameter scaling and radiation efficiency of microearthquakes along the Irpinia fault zone in southern Apennines, Italy. J Geophys Res Solid Earth. https://doi.org/10.1002/2013JB010116

Authors and Affiliations

Sotiris Valkaniotis[1] · Vincenzo De Novellis[2] · Athanassios Ganas[3] · Eugenio Sansosti[2] · Vincenzo Convertito[4] · Pierre Briole[5] · Varvara Tsironi[3,6] · Ilektra Karasante[7] · Ioannis Karamitros[3]

✉ Athanassios Ganas
aganas@noa.gr

Sotiris Valkaniotis
valkaniotis@yahoo.com

Vincenzo De Novellis
vincenzo.denovellis@cnr.it

Eugenio Sansosti
eugenio.sansosti@cnr.it

Vincenzo Convertito
vincenzo.convertito@ingv.it

Pierre Briole
briole@ens.fr

Varvara Tsironi
vtsironi@noa.gr

Ilektra Karasante
ile.karasante@noa.gr

Ioannis Karamitros
jkaram@noa.gr

[1] Department of Civil Engineering, Democritus University of Thrace, 67100 Xanthi, Greece

[2] National Research Council (CNR), Istituto per il Rilevamento Elettromagnetico dell'Ambiente (IREA), Via Diocleziano 328, Naples, Italy

[3] National Observatory of Athens, Institute of Geodynamics, Lofos Nymfon, Thission, 11810 Athens, Greece

[4] Istituto Nazionale di Geofisica e Vulcanologia (INGV), Osservatorio Vesuviano (OV), Via Diocleziano 328, Naples, Italy

[5] Laboratoire de Géologie - UMR CNRS 8538, Ecole Normale Supérieure de Paris, PSL Research University, 24 Rue Lhomond, 75005 Paris, France

[6] National Observatory of Athens, Institute of Geodynamics, Lofos Nymfon, Thission, 11810 Athens, Greece

[7] National Observatory of Athens, Institute for Astronomy, Astrophysics, Space Applications and Remote Sensing (IAASARS), Vas. Pavlou and I. Metaxa, Penteli, 15 236 Athens, Greece